Journal of Power Sources 438 (2019) 227045

Contents lists available at ScienceDirect

Journal of Power Sources

journal homepage: www.elsevier.com/locate/jpowsour

Nitrogen and phosphorus co-doped silkworm-cocoon-based self-activated porous carbon for high performance supercapacitors

Yakun Wang [a,1], Mengke Zhang [a,1], Yang Dai [a,**], Hui-Qiong Wang [c,d], Huaiyu Zhang [b], Qianqian Wang [a], Wenbo Hou [a], Hao Yan [a,*], Wenrong Li [a,***], Jin-Cheng Zheng [c,d,****]

[a] Department of Chemical Engineering, School of Environmental and Chemical Engineering, Institute for Sustainable Energy, Shanghai University, Shangda Road 99, Shanghai, 200444, China
[b] Mork Family Department of Chemical Engineering and Materials Science, University of Southern California, Los Angeles, CA, 90089, United States
[c] Department of Physics, Collaborative Innovation Center for Optoelectronic Semiconductors and Efficient Devices, Xiamen University, Xiamen, 361005, China
[d] Xiamen University Malaysia, 439000, Sepang, Selangor, Malaysia

HIGHLIGHTS

- N/P co-doped porous carbon is prepared from silkworm cocoon and phytic acid.
- As the electrode active material for high performance supercapacitor.
- 317 F g^{-1} (482 F cm^{-3}) at 1 A g^{-1}, and 159 F g^{-1} (242 F cm^{-3}) at 50 A g^{-1}
- A high areal capacitance of 2.44 F cm^{-2} can be obtained.
- Flexible supercapacitor delivers maximum 19.6 Wh kg^{-1} and 17.5 kw kg^{-1}.

ARTICLE INFO

Keywords:
Porous carbon
Capacitive performance
Semi-solid state supercapacitor
Flexible devices
Silkworm cocoon
Biomass

ABSTRACT

N/P co-doped porous carbon is prepared from biomass (silkworm cocoon) and natural product (phytic acid) by an eco-friendly self-activation approach. Owing to the rational pore structure, and abundant pseudocapacitive active sites of heteroatom doping, the prepared Cheese-brick-like porous carbon presents outstanding performances. The optimized S2 sample delivers both high gravimetric capacitance and volumetric capacitance of 317 F g^{-1} (482 F cm^{-3}) at 1 A g^{-1}, and an impressive capacitance of 159 F g^{-1} (242 F cm^{-3}) at a high current density of 50 A g^{-1} in 1 M H_2SO_4. Also, the thick electrode (10 mg cm^{-2}) can deliver a high areal capacitance up to 2.44 F cm^{-2} at 10 mA cm^{-2} and 1.29 F cm^{-2} at 500 mA cm^{-2}. Additionally, the porous carbon based flexible symmetric supercapacitor (1.4 V) can deliver a remarkable 19.6 Wh kg^{-1} (29.8 Wh l^{-1}) at 350 W kg^{-1}, and 9.6 Wh kg^{-1} (14.6 Wh l^{-1}) at 17500 W kg^{-1}, respectively, as well as outstanding cyclic longevity (~98% capacitance retention after 10000 cycles). These attractive performances enable a wonderful potential of our porous carbon applied in supercapacitors for wearable electronics and other energy storage devices.

1. Introduction

With characters of high power and long cyclic life, electrochemical supercapacitors (ECs), play an essential role of bridging the gap between batteries and traditional capacitors. ECs can be mainly classified into electrical double layer capacitors (EDLCs) and pseudocapacitors by different charge storage mechanisms. EDLCs store the charge originated from the electrosorption of ions at the electrode/electrolyte interface, while pseudocapacitors utilize reversible fast faradaic reactions involving interfacial electron transfer between the electrode and

* Corresponding author.
** Corresponding author.
*** Corresponding author.
**** Corresponding author. Department of Physics, and Collaborative Innovation Center for Optoelectronic Semiconductors and Efficient Devices, Xiamen University, Xiamen, 361005, China.
E-mail addresses: dy1982@shu.edu.cn (Y. Dai), hao-yan@shu.edu.cn (H. Yan), Liwenrong@shu.edu.cn (W. Li), jczheng@xmu.edu.cn (J.-C. Zheng).
[1] These authors contribute equally to this paper.

https://doi.org/10.1016/j.jpowsour.2019.227045
Received 14 June 2019; Received in revised form 14 August 2019; Accepted 19 August 2019
Available online 26 August 2019
0378-7753/© 2019 Elsevier B.V. All rights reserved.

electrolyte. In whatever types, the electrode material is one of the most paramount components, mainly determining the performances. Among the electrode materials, porous carbon is most widely applied due to its relatively low cost, long cyclic durability, high power capability and it is environmentally friendly [1–4]. Considerable efforts have been devoted to prepare porous carbon for supercapacitor. A wide range of porous carbons derived from biomass [2–12], such as bristlegrass seeds [2], bamboo [3], Jujube [5], silkworm cocoon [6–9], pistachio shell [10], seaweed [11] banana fiber [12] and so on, have been widely investigated as the potential electrode materials. Some of the biomass derived porous carbon contain heteroatoms, such as oxygen (O), phosphorus (P), nitrogen (N), sulfur (S) and P, N codoped [1,13–17]. It has been proved that the incorporation of heteroatoms in porous carbon can greatly enhance the capacitive performance. Particularly, N doping has been widely reported to improve the performance by altering the electrical conductivity, chemical reactivity, microstructure, as well as participating in the faradaic process [14]. As a naturally sustainable biomass, silkworm cocoon derived porous carbons, which are rich in nitrogen content, have been widely explored as the potential electrode materials for supercapacitor. In order to obtain excellent capacitive performances, cocoon derived or their composite porous carbons with various preparation approaches have been well investigated, such as microporous carbon nanoplates from regenerated silk fibroin-KOH film [17], carbon from staged KOH activation [7], nitrogen doped graphene by activation of HNO_3 [6], Silk/CNT composite [9], Silk/GO carbon aerogel [8]. Those interesting reports clearly demonstrate the silk cocoon is a promising raw material for supercapacitor electrode materials. An impressive high capacitance of 408 Fg^{-1} can be achieved with ultrahigh specific surface area of 3841 $cm^{-2}g^{-1}$ by staged KOH activation [7]. However, such a high surface area may result in lower density, leading to lower volumetric capacitance, which is considered as an important metric to evaluate the performance of the electrode material [18,19]. Additionally, although the common used activated agents (such as KOH, NaOH) is effective, they may corrode the furnace at high temperature [10].

In this paper, we develop a facile method to prepare N/P-co-doped porous carbon for supercapacitor electrode materials, employing the natural products of Silkworm cocoon and phytic acid (PA) as the raw materials. Silkworm cocoon provides the N and the mainly carbon source with interesting network structure. PA, as a nontoxic molecular compound, which presents in most of legumes, including nuts, soy beans, and corns, plays the roles of P-doping source, activated agent, as well partial carbon source. It is a self-activation and self-co-doping approach to prepare porous carbon, which is simple, mild, eco-friendly and cost-effective. The resulting Cheese-brick-like carbons exhibit microporous texture (with a medium surface area of 500–2000 $m^2 g^{-1}$) with high N and P co-doped. The aforementioned porous carbon, taking advantage of N, P heteroatoms incorporation, enhancing the capacitive performance. The S2 sample shows an outstanding performance, achieving both high gravimetric capacitance and volumetric capacitance of 317 F g^{-1} (482 F cm^{-1}) at 1 A g^{-1}, and an impressive capacitance of 159 F g^{-1} (242 F cm^{-1}) at a high current density of 50 A g^{-1} in 1 M H_2SO_4. To demonstrate its practicality, a flexible H_2SO_4/PVA based symmetric supercapacitor was fabricated. With distinct flexibility, it can extend the potential window up to 1.4 V, delivering a remarkable 19.6 Wh kg^{-1} at 350 W kg^{-1}, and 9.6 Wh kg^{-1} at 17500 W kg^{-1}, as well as outstanding cyclic longevity (~98% capacitance retention after 10000 cycles).

2. Experimental

2.1. Preparation of samples

N, P co-doped porous carbon was synthesized by mixing 1.5 g silk cocoon with different mass ratio (S1:0.5, S2: 1, S3: 1.5) of Phytic acid (70% water solution, Alladdin) in a flask. Then, the mixture was evaporate to dryness in a drying oven at 80 °C. After that, the mixture was heated at 10 °C min^{-1} in a tube furnace for 2 h under the flowing N_2 at 900 °C. For comparison, the sample without phytic acid (S0) also prepared. The as-prepared sample was ground and rinsed with 0.5 M HCl solution and then ultrapure water for several times.

2.2. Characterization

The surface morphologies were observed by a Hitachi S4800 microscope. The microstructure was visualized on a JEOL JEM-2100F microscope. A Rigaku D/max-2600PC diffractometer (XRD) with nickel-filtered Cu Kα radiation (λ = 1.5418 Å) was used to determine the structure of the samples. Raman spectra was obtained by a Renishaw Reflex (λ = 532.5 nm). Nitrogen isotherm was collected by a Micromeritics (ASAP 2020) at 77 K. Before testing, the sample was outgassed at 250 °C for 12 h. X-ray photoelectron spectroscopy (XPS) was performed on a XPS System (Thermo Fisher Scientific ESCALAB 250Xi). A Shirley background was removed from the spectra before deconvolution. A four point probe meter (SX1944, Suzhou Telecommunication Instrument) was used to determine the electrical conductivity. 90 wt% of the sample and 10 wt% Polytetrafluoroethylene (PTFE) were blended and pressed at 25 MPa to form discs (ϕ30 mm, thickness of 50 μm). For comparison, the commercial carbon YP-50 is also evaluated.

2.3. Electrochemical evaluation in three-electrode cell

Usually, PTFE and PVDF based process are two most common electrode-fabrication methods for performance evaluation. In order to test the high mass loading electrode, the PTFE based process is easy to implement. The disc-shaped-electrode is fabricated by mechanical pressing of the pre-mixed slurry. To form a uniform slurry, the sample (80 wt %) powder, PTFE binder (10 wt %, 60 wt % in H_2O, Aldrich) and conducting carbon (super-p, 10%) were thoroughly mixed. The working electrodes were prepared by pressing the electrode onto a stainless mesh (400 mesh) and measured in a conventional three-electrode cell with 1 M H_2SO_4 electrolyte. The Ag/AgCl and Pt foils (4 cm^2) were used as the reference electrode and counter electrode, respectively. The mass loading is 2.00–3.00 mg cm^{-2}.

2.4. Fabrication of flexible two-electrode symmetric supercapacitor

The electrodes were fabricated by cast coating the slurry onto current collector of CNT cloth (~0.7 × 1.6 cm, 17 μm thick) with a mass loading of 2.00–3.00 mg cm^{-2}. After drying and rolling depression, the sol gel electrolyte (PVA/H_2SO_4) was spread onto the electrodes. Two gel coated electrodes were pasted together in a sandwiched way. After the solidifying the electrolyte, the supercapacitor is well prepared. Cyclic Voltammetry (CV) at various scan rates and galvanostatic charge-discharge (GCD) with different current densities were recorded on a potentiostat–galvanostat (CHI 660C) instrument. The contribution to the capacitance of the current collector has been deducted.

2.5. Calculations

The specific capacitance was calculated from the CVs or the GCD curves, based on the equations [19]:

$$C_g = \int IdV/(vmV) \quad (1)$$

$$C_g = It/(mV) \quad (2)$$

$$C_v = C_g * \rho \quad (3)$$

Here, C_g is the gravimetric capacitance (Fg^{-1}), I is current (A), $v$is the scan rate (V/s), m is mass (g), V is potential range, t is discharging time, C_v is the volumetric capacitance (F cm^{-3}), and ρ is the density of each

electrode films.

The energy density E (Wh kg^{-1}), and power density P (W kg^{-1}) of the symmetric two-electrode cell were calculated based on the GCD curve by the following equations:

$$C_1 = It/(m\ \Delta V) \quad (4)$$

$$E = C_1\ \Delta V^2/(3.6 \times 8) \quad (5)$$

$$P = 3600E/t_2 \quad (6)$$

$$E_v = E^*\rho \quad (7)$$

$$P_v = P^*\rho \quad (8)$$

Where C_1 is the single electrode gravimetric capacitance of the two-electrode cell, I is the applied current density based on the single electrode, m is mass based on a single electrode, ΔV is the effective potential range during discharge, t_2 is the discharging time (s), E is the gravimetric energy density, and E_v is the volumetric energy density, P is the gravimetric power density, P_v is the volumetric energy density, and ρ is the density of each electrode films.

3. Results and discussion

3.1. Material preparation and characterization

Fig. 1 (a)-(d) present the SEM image of the resulting samples. After activation and carbonization, the shape of the particles turns out to be irregular flakes, with dimension of 10–20 μm. Compared to the S0

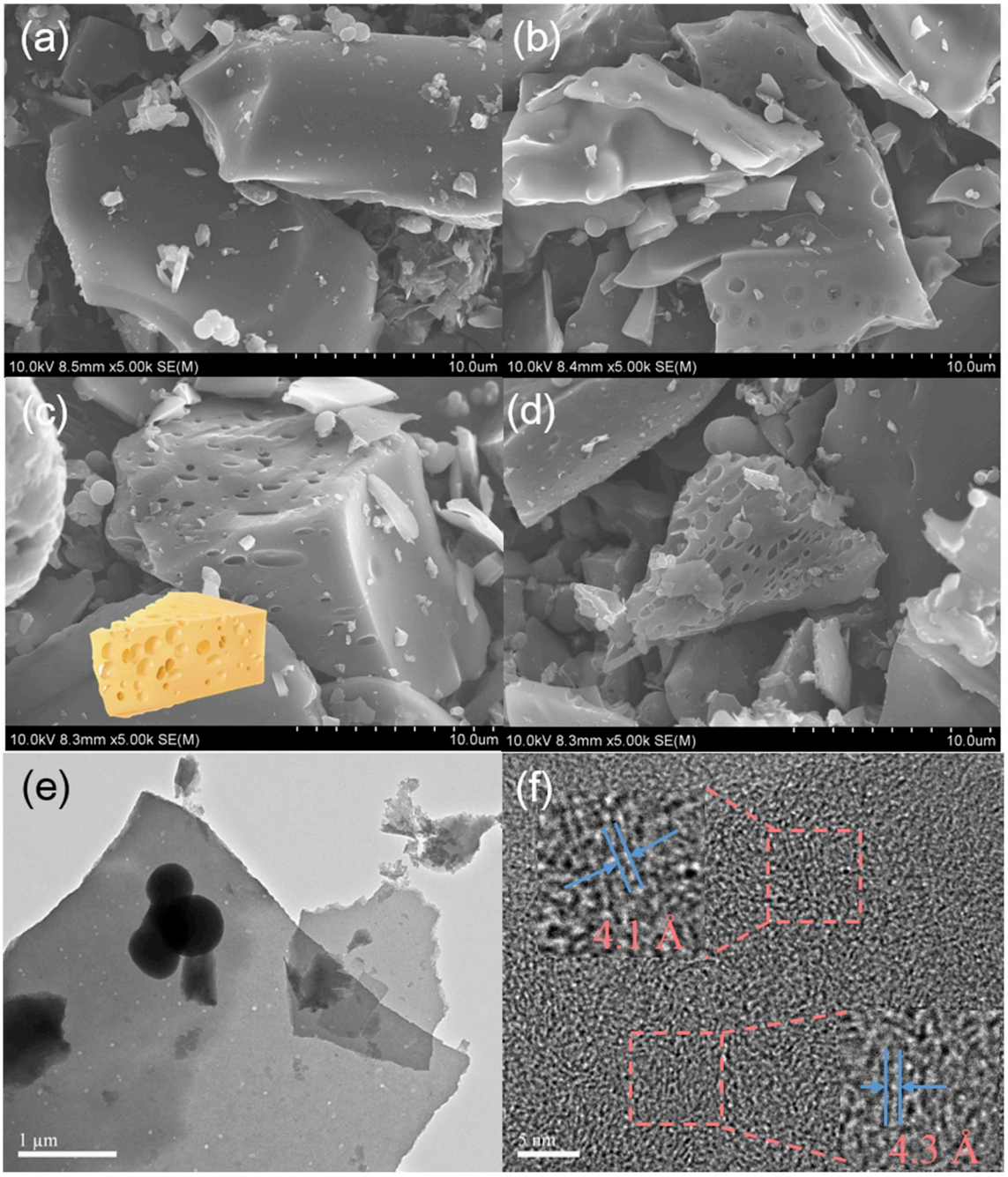

Fig. 1. SEM images of the prepared samples (a) S0 (b) S1(c) S2 (d) S3, and inset in (c) is a piece of cheese for comparison. TEM (e) and HRTEM (f) of the sample S2. The inset in (f) is fast Inversed Fourier transformed (IFFT) patterns of the selected square area HRTEM image.

(without PA), the particles of other samples possess some "air bubbles"similar to the cheese bricks (inset in Fig. (d)). The "air bubbles"may originated from the decomposition of the phytic acid during the carbonization process. The cheese-brick-like porous structure of the particles with open pores may act as ion-saving container, in favor of fast reaction. The sample S2 is further verified by the TEM images (Fig. 1e–f). Similar to former reports, the particle can be exfoliated into lamella-like layers after sonication, with hundreds nanometers thickness. And small pores with 50–100 nm can be observed in the layers. This structure may be induced from self-assemble of the silk fibroin and PA [17]. Inside the particle, it basically exhibits amorphous structure with an irregular atomic arrangement (Fig. 1f). However, it also presents some fringes of lamella-like structure with a d-spacing~4 Å, as shown in the inset picture.

XRD patterns of the prepared samples are plotted in Fig. 2 (a). Two broad peaks at 22°and 43° with low intensity can be indexed as the (002) and (100), revealing the amorphous graphitic structure of the samples [20]. Note that, the samples exhibit diffraction peaks (002) shifting from 26.54° of graphite to lower values of 22.3–24.4°, which suggests the expansion of the interlayer spacing of the prepared samples. This may be due to the distortion of the graphitic planes caused by N, P doping. On careful observation, this expansion increases along with the increasing of PA ratios. It has been reported that P is likely to incorporate on the graphene edges, which may enhance the interlayer spacing [1]. Therefore, the expansion of the d-spacing may be attributed to the more P-doping. Fig. 2b shows the Raman spectrum of the samples. There are two obvious peaks at around 1320 and 1580 cm^{-1}, corresponding to the D-band and G-band, respectively [21]. The high integral Ig/Id value verifies partial graphitization structure of the samples, suggesting the samples may possess good electrical conductivity [10]. Among the S0–S3 samples, the S2 has the highest Ig/Id value, implying the highest degree of graphitization. The electrical conductivity are also measured by four-point probe method [10]. The values turn out to be 2.1 (S0), 1.2 (S1), 2.6 (S2), and 2.4 S cm^{-1}(S3), compared to 1.2 S cm^{-1} of the commercial YP-50. The satisfactory electrical conductivity could be due to the amorphous graphitic structure or P, N co-doping.

The N_2 adsorption isotherms and the pore size distribution for the four samples are presented in Fig. 2c and d, respectively. And the detailed information is presented in Table 1. The S0 sample without PA exhibits a small BET area of 24 $m^2 g^{-1}$, revealing that the PA is an effective activated agent. At high temperature, PA is supposed to release the phosphoric acid anions which could act as an acid catalyst in promoting bond cleavage reactions with the silk protein and formation of crosslinks [1,17].

The three samples (S1, S2, S3) exhibit medium values of the BET area (500–2000 m^2g^{-1}), mainly composing of micropores. From the shape of the isotherms (I/IV type curves), the PA activated samples (S1, S2, S3) can be assigned to the microporous and mesoporous (with an obvious hysteresis loop in the high pressure range) character [22]. However, the BET values do not increase with the increasing of amount of PA. It is notable that the sample S2 possesses the highest pore volume. The pore size distributions are exhibited in Fig. 2d. The pores for PA activated samples are mainly composed of micropores (<2 nm), especially the sub-nanopores (<1 nm), which are considered to dominantly provide enhanced capacitance [5]. A small part of mesopores are also included in the samples (S1, S2, S3), which can be functional as pathways for ions transport [5]. In addition, macropores are not detected in the sample. The low mesopores/macropores contain can make sure the high density

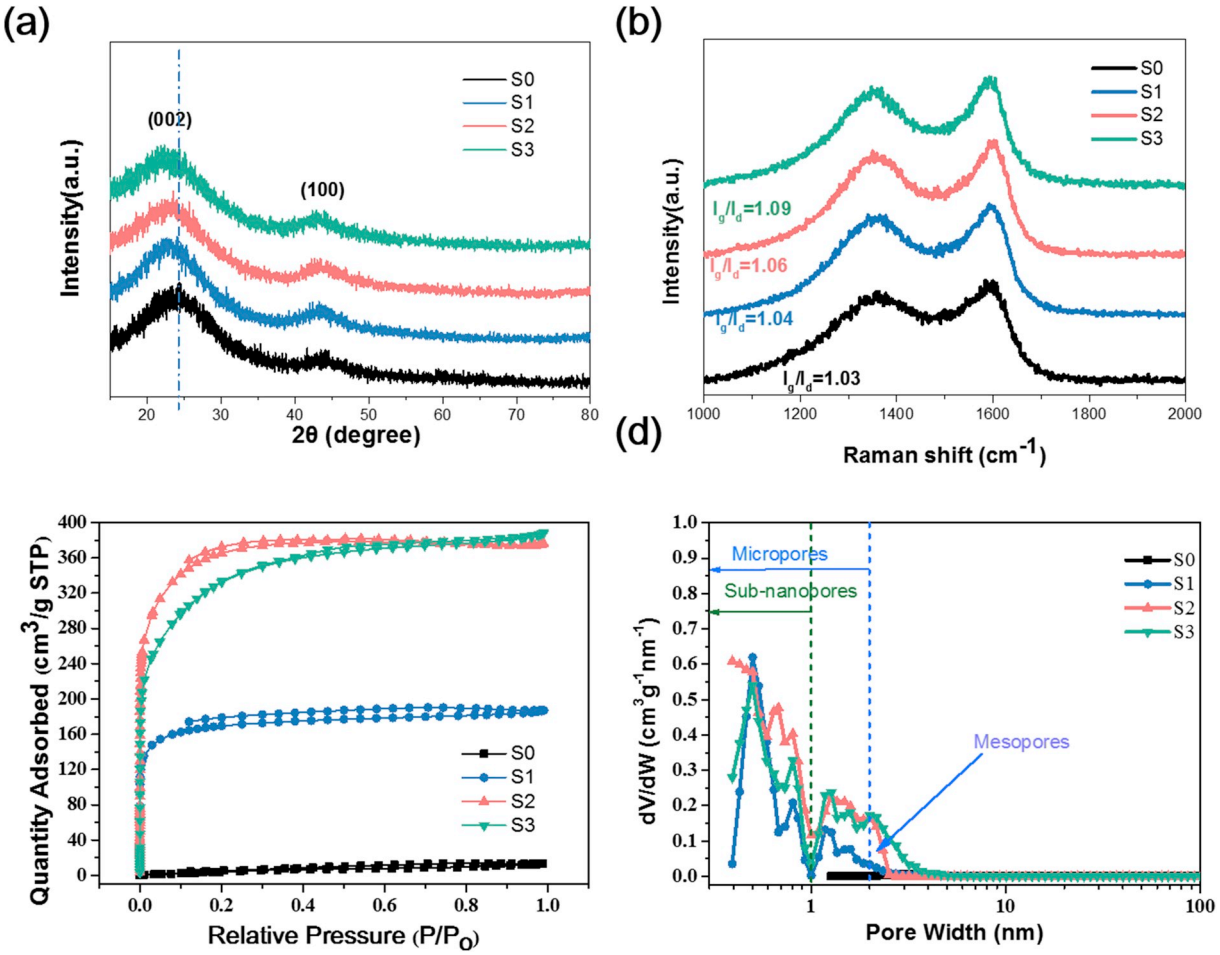

Fig. 2. Structural characterization of the as-prepared samples, (a) XRD patterns (b) Raman spectrum (c) Isothermal curve of N2 adsorption. (d) Pore distribution.

Table 1
XPS data, BET analysis, and pore size distribution of the samples.

Sample	Mass ratio Cocoon/PA	XPS				$S^a_{BET}(m^2g^{-1})$	$S^b_{mic}(m^2g^{-1})$	$V^c_{total}(cm^3g^{-1})$
		P%	C%	N%	O%			
S0	0	0	85.50	4.08	10.42	24.36	12.27	0.02
S1	1:0.5	1.55	84.9	3.08	10.47	567.99	495.58	0.28
S2	1:1	1.63	85.31	3.65	9.41	1247.60	1083.82	0.58
S3	1:2	2.90	76.43	1.98	18.69	1168.07	805.20	0.60

Specific surface area determined according to BET method. b. From T-plot method. c. Total pore volume.

of the porous carbon.

To determine the bonding information and chemical composition, the samples were examined by XPS (Fig. 3 and Table 1). Table 1 generalizes the composition of the prepared samples. Both the P and N are contained in the three samples. It can be also observed that the contents of P element increase with the enhancement of PA. The N 1s, P 2p of the S2 sample are further analyzed and shown in Fig. 3. The N 1s can be mainly deconvoluted into four peaks as 398.5 eV, 400.2 eV, 401.2 eV and 402.1 eV, which correspond to the pyridinic N, pyrrolic N, graphitic N and oxidized N, respectively. As shown in Fig. 3 (b), the P 2p can be deconvoluted into the tetrahedral C–PO_3 (133.3 eV) and C_3–PO (132.2 eV). The P-containing groups may be located on the edge of the graphene layers, which is consistent with the XRD results of increasing the interlayer spacing (Fig. 2a) [1].

3.2. Electrochemical performances in three-electrode-cell

Based on the material characterization, the porous carbon (S1, S2, S3) with abundant active reaction sites, rational pore structure, and excellent electrical conductivity are observed, thus outstanding electrochemical performances is expected to be achieved.

To evaluate the performance of the prepared samples as electrode materials for supercapacitors, they were examined in a three-electrode cell with 1.0 M aqueous H_2SO_4 electrolyte. Fig. 4a displays the typical CV profiles of the samples at a medium rate of 10 mV s^{-1}. The PA activated samples (S1, S2 and S3) present much larger areas, indicating the large capacitance enhancing. This could be attributed to the enhancing of EDL dominated capacitance while the BET surface raises after the PA activation, illustrating the important role of PA. Samples S1, S2 and S3 present a symmetric rectangular shapes, indicating nearly ideal capacitive performance. The curves also exhibit a set of broader humps at around 0.4 V vs Ag/AgCl, suggesting the coexistence of pseudocapacitance along with the electrical double layer capacitance. Without PA activation, the S0 shows an asymmetric wedge-shaped curve, indicating poor capacitive performance. It is noteworthy that the operational potential window of the prepared sample is 1.2 V, which is higher than other porous carbon using H_2SO_4 based electrolytes. The reason can be attributed to the bonded N- and P- based surface groups, which can accept the protons to prevent the water splitting to a certain extent. As shown in Fig. 4b, it plots the galvanostatic charge-discharge (GCD) profiles at 1 A g^{-1} for the samples. The curves are shown to be symmetric-slope-shaped, which is a typical index of capacitive behavior [23]. Calculated from the CVs and GCD profiles, the S2 shows the best performances. To further understand the capacitive behavior, electrochemical impedance spectroscopy (EIS) is further employed to test the sample based electrodes (Fig. 4c).

The EIS is measured at open circuit voltage from 0.1 to 10^6 Hz. The Nyquist plots display small semi-circles at the high frequency region and straight lines in the low frequency region. The line denotes Warburg impedance, which comes from the ion diffusion of the electrolyte. It is accepted that the more vertical of the straight line, the more ideal capacitive performance of the porous carbon. Thus, the PA activated carbon (S1, S2, and S3) with almost vertical lines suggest ideal capacitive performance. On the contrary, the deviated vertical line of the S0 indicates much poor capacitive behavior, which is in accord with the asymmetric CV curve. The semicircle represents charge transfer resistance from the interface of electrode/electrolyte. The existence of small semicircles reveals the pseudocapacitive behavior of the porous carbon [3]. From the plots, the S1 exhibits most vertical line to the x-axis with lower transfer resistance compared to other plots, which is consistent with the electrochemical performances results (Fig. S1).

Fig. 4c shows the GCD profiles recorded at different current densities of sample S2. The calculated gravimetric (C_g) and volumetric (C_v) capacitances based on the GCD results versus current density are presented in Fig. 4d. The specific capacitances are calculated to be 317 F g^{-1}, (482 F cm^{-1}) at low current density of 1 A g^{-1}. Even at high discharge rate of 50 A g^{-1}, it still can deliver a high capacitance of 159 F g^{-1} (242 F cm^{-1}), demonstrating excellent rate performance. It is worth mentioning that, the values of the volumetric capacitances are much higher due to the high density of the sample. Table S1 and Fig. 4f present the capacitive performances and methods of reported silk-cocoon-derived and other biomass derived porous carbons. Compared to other silk-cocoon-derived carbons, our method is facile and effective. Also, the volumetric capacitance value is relatively higher compared to other biomaterials derived carbons, such as porous carbon from jujube [5], seaweed [11], Perilla frutescens leaves [13], soybeans [24], Auricularia

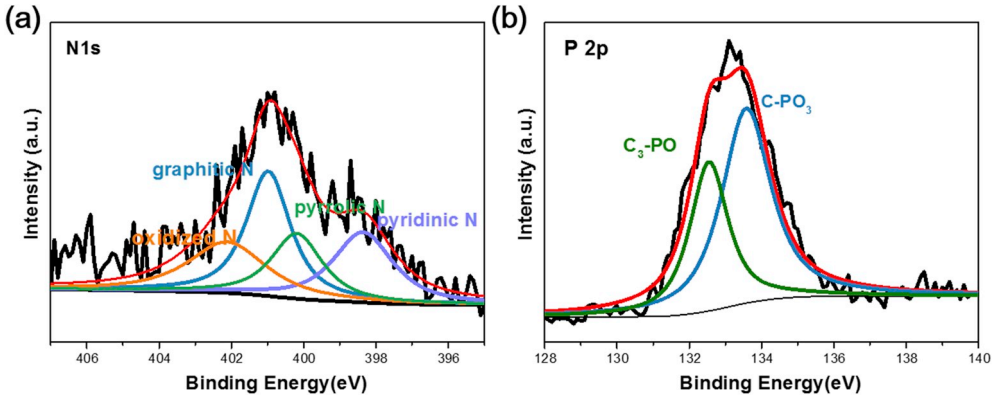

Fig. 3. XPS spectra of S2 sample (a) N1s and (b) P2p.

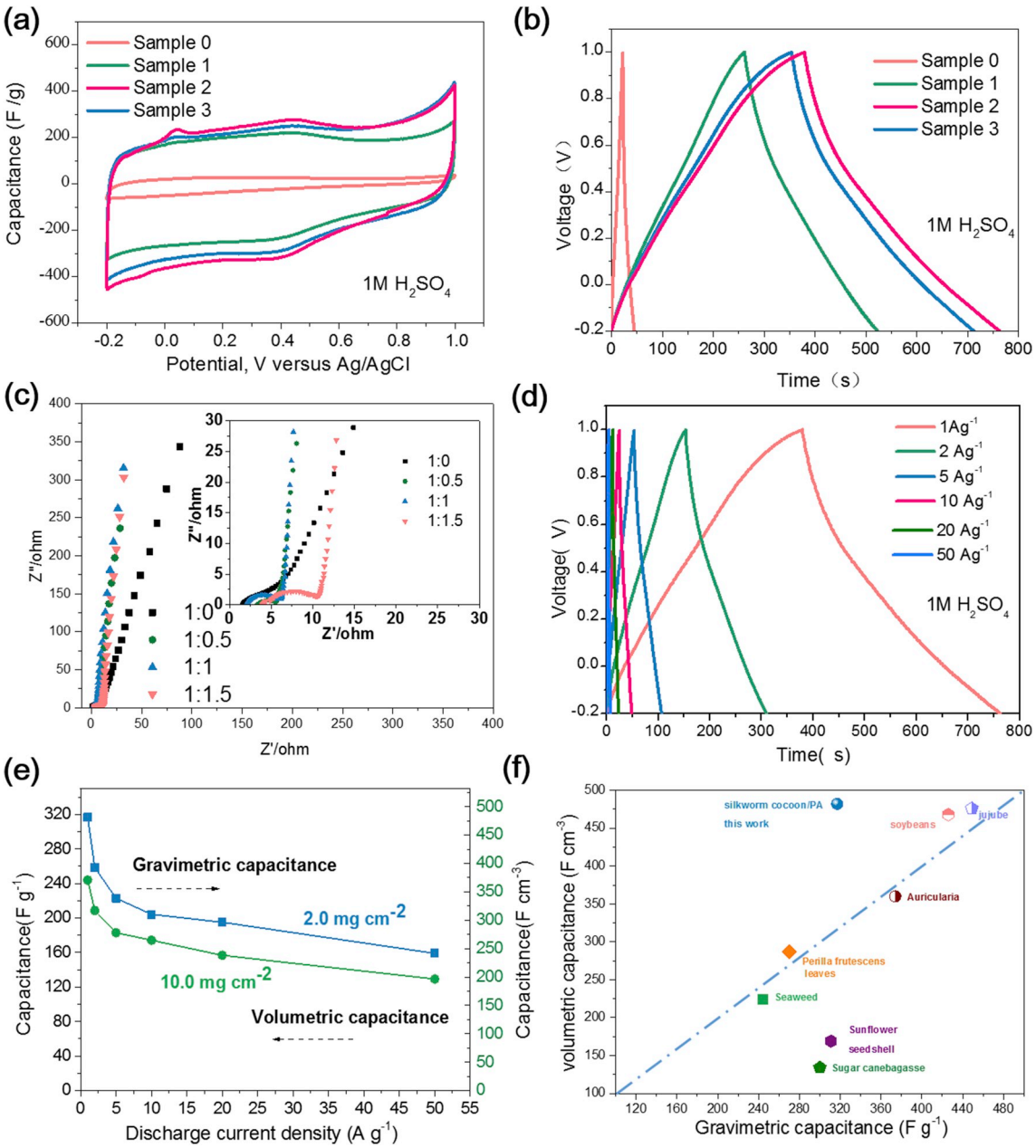

Fig. 4. Electrochemical performance of different samples (−0.2–1.0 V vs. Ag/AgCl, 1 M H_2SO_4) (a) CV profiles at 10 mv s^{-1}, (b) GCD curves at 1 A g^{-1} (c) Electrochemical impedance spectrum (EIS) of the different samples based electrode (inset is magnified region at high frequency). (d) GCD curves of the S2 sample at different current densities. (e) Plot of capacitance versus discharge current density of S2 (f) Comparison of the specific capacitances of S2 with former reports.

[25] and sugarcane bagasse [26]. The high volumetric values can be attributed to the high density of the sample. The high density could be ascribed to the micropores dominated texture, without abundant mesopores or macropores. High mass loading and areal capacitance are two another paramount metrics to evaluate the capacitive behavior. Fig. S2 shows the capacitive performances of the high mass loading electrode (S2, 10 mg cm^{-2}). The outstanding capacitive behavior can be seen from the CV and GCD curves (Fig. S2 a, b). Even at a high rate of 500 mv s^{-1} and a high current density of 50 Ag^{-1}, the curves still turn out to be well defined rectangle and symmetric slopes, respectively. Indeed, the thick electrode can exert a high capacitance of 244 and 129 F g^{-1}, at 1 and 50 A g^{-1} (3s discharge response), respectively. This means the areal capacitance can be delivered up to 2.44 and 1.29 F cm^{-2}, at 10 mA cm^{-2} and high current density of 500 mA cm^{-2}, respectively, demonstrating the potential application of this material in wearable power sources.

The distinct performance can be attributed to unique structure of the material. Highly conductive N, P co-doped graphitic lamella-like nanolayers (Fig. 1e) stacking together to form micro-sized particles, facilitates the electron transfer and ensures the packing density. Balance of sub-nanopores, micropores and mesopores plays a paramount role in capacitive performance (Fig. 2d) Abundant sub-nanopores and micropores provide a part of capacitance. And the active N, or P species may generate along the pores to form active sites for fast pseudocapacitive reactions. The sufficient mesopores can enable facile transport of electrolyte ions to access the active surfaces and active sites. Thus, the effective conducting-network of electron and ion can be formed to achieve the excellent rate-performance.

In addition, the contribution of the capacitance is another important issue. Since the sample with relatively low surface area (only ~1000 m^2 g^{-1}) could not afford to provide such a high capacitance (~320 F g^{-1}) by electrical double layer. The mainly capacitance contributor should be the pseudocapacitance. The co-doping of N, P

containing functionalities may enhance the capacitance. The N- and P-, based functional groups could mainly directly produce pseudocapacitance by redox reactions. The reactions are proposed as below [1,13,27].

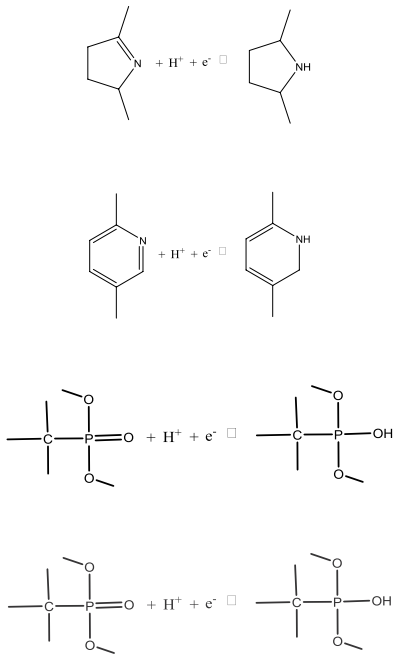

Furthermore, linking the capacitive results (Fig. 3 a, b) to the XPS element content results (Fig. 3b), it seems the N content active sites may make greater contribution to the capacitance than P active sites.

3.3. Electrochemical performance of flexible symmetric two-electrode-cell

We have proved the outstanding performance of the prepared porous carbon (S2) using PTFE binder based process, especially the high mass loading electrode. Unfortunately, the PTFE binder based process is not so compatible with the PVA based electrolyte. And the PTFE binder based electrode is not flexible enough for wearable electronic application. Thus, the-slurry-coating method is applied to fabricate the flexible supercapacitor.

To verify the practicality of the prepared sample for device application [28–30], a flexible semi-solid-state supercapacitor based on S1 is fabricated. CVs at 10 mV s^{-1} with different bending angles are carried out to test the flexibility of the device (Fig. 5a). The rectangular shaped CVs exhibit almost overlapped curves, indicating the flexibility and excellent capacitive performance of the device. In addition, the operational voltage can be extended to 1.4 V in the two-electrode-device, which will largely contribute to enhance the energy density. Fig. 4b displays the GCD plots recorded with different current densities. All of the curves show nearly symmetric slashes, revealing the good capacitive behavior of the device. The cell presents a high capacitance of 288 F g^{-1} at 1 A g^{-1}. This value is slightly lower than that of measured in three-electrode-cell (316 F g^{-1}), which may be due to the electrode coupling and relative slower kinetic of the semi-solidstate-electrolyte. Impressively, the cell can deliver a high capacitance of 142 F g^{-1} at 50 A g^{-1}, with a high capacitance retention ratio 50A/1 A of 49% [29]. The excellent performances could originate from the compatibility between the active material and current collector. The Ragone plot in Fig. 5c presents the outstanding capacitive performance of the flexible supercapacitor. High energy density of 19.6 Wh kg^{-1} at 350 W kg^{-1}, and 9.6 Wh kg^{-1} at 17500 W kg^{-1} (29.8 Wh l^{-1} at 532 W l^{-1}, and 14.6 Wh

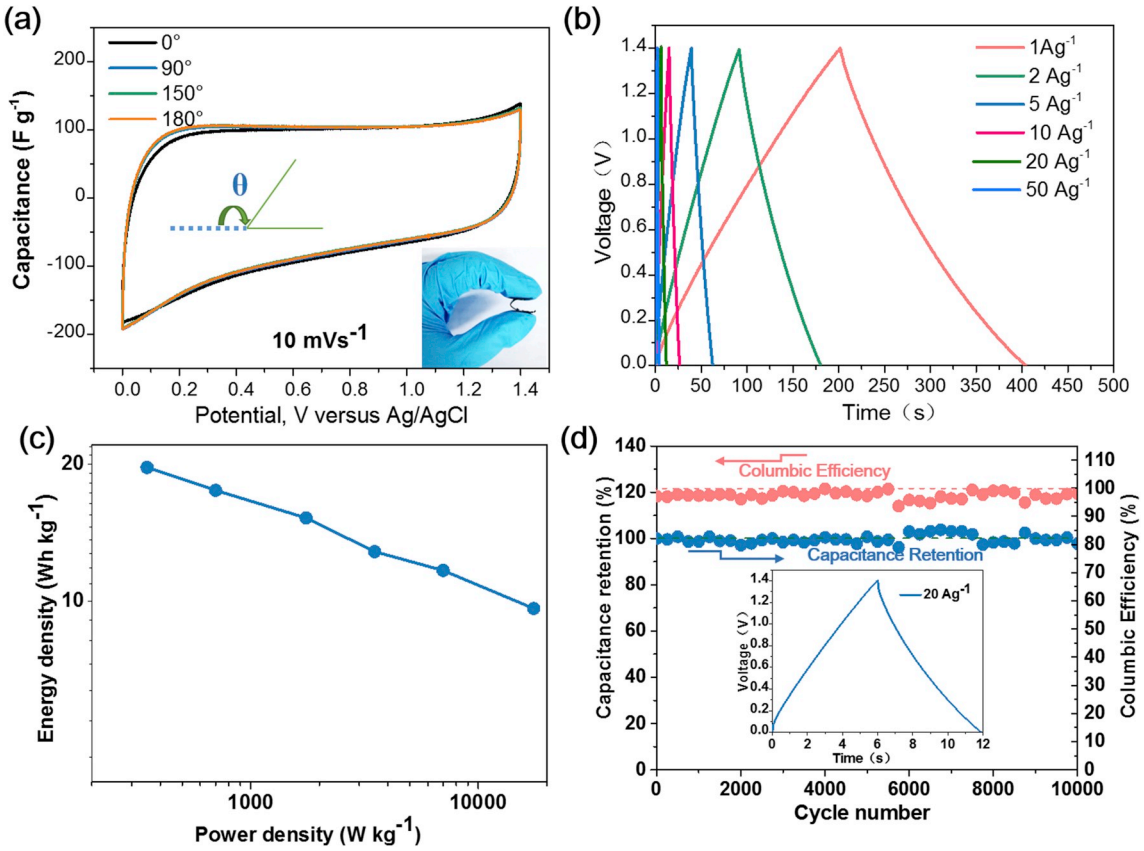

Fig. 5. CV curves at 10 mV s^{-1} for the flexible supercapacitor subjected to different bending (inset is the picture of bended flexible supercapacitor). (b) GCD curves at 1–50 A g^{-1}. (c) Ragone plot. (d) Cyclic performance at 20 A g^{-1}. The inset is the GCD curve at 20 A g^{-1}. The blue and red discs denote capacitance retention and columbic efficiency, respectively. (For interpretation of the references to colour in this figure legend, the reader is referred to the Web version of this article.)

l^{-1} at 26600 W l^{-1}) can be achieved. For supercapacitor, long cyclic capability is a paramount feature. Indeed, our flexible supercapacitor can keep a capacitance over 97.8% after 10,000 cycles at 20 Ag^{-1}, implying superb electrochemical cycling stability. Such values are so competitive compared to some flexible supercapacitors (Table S1). Furthermore, the performance can be improved by optimizing the fabricating process and device design.

4. Conclusion

In this paper, we developed a facile, mild, eco-friendly and cost-effective self-activation method to prepare N/P-co-doped porous carbon. The prepared sample (S1) shows cheese-brick-shaped particles assembled with laminar carbon layers. Attributed to the expanded interlayer spacing of (002), rational pore structure, abundant active sites of P, N-co-doing, the samples exhibit excellent capacitive performances. The S2 sample achieves both high gravimetric capacitance and volumetric capacitance of 317 F g^{-1} (482 F cm^{-1}) at 1 A g^{-1}, and an impressive capacitance of 126 F g^{-1} (242 F cm^{-1}) even at a high current density of 50 A g^{-1} in 1 M H_2SO_4. Additionally, the porous carbon based a flexible symmetric can deliver a remarkable 19.6 Wh kg^{-1} at 350 W kg^{-1}, and 9.6 Wh kg^{-1} at 17500 W kg^{-1}, respectively, as well as outstanding cyclic longevity (~98% capacitance retention after 10000 cycles). Considering the abundance and sustainability of the silkworm and phytic acid, together with the easy controlled self-activation process, the N, P-co-doped porous carbon will also be possibly used in other energy storage aspects, such as batteries, catalyst for fuel cell, or water splitting, and so on. Therefore, our work here provides a simple, cost-effective, and green approach to prepare P, N-codoped porous carbon for energy storage applications.

Acknowledgements

Financial support from the National Natural Science Foundation of China (No. 21103109, No. 21176152, No. 21373137, No. 51661135011), the support provided by China Scholarship Council (CSC) during a visit of Yang Dai (CSC No. 201806895011) to Brookhaven National Laboratory is acknowledged. The beam time and technical supports at the beamline stations BL14B1 and BL14W1, at the Shanghai Synchrotron Radiation Facility (SSRF) (Shanghai, China) are appreciated.

Appendix A. Supplementary data

Supplementary data to this article can be found online at https://doi.org/10.1016/j.jpowsour.2019.227045.

References

[1] T. Panja, D. Bhattacharjya, J.-S. Yu, J. Mater. Chem. 3 (2015) 18001–18009.
[2] W. Zhou, S. Lei, S. Sun, X. Ou, Q. Fu, Y. Xu, Y. Xiao, B. Cheng, J. Power Sources 402 (2018) 203–212.
[3] Y. Gong, D. Li, C. Luo, Q. Fu, C. Pan, Green Chem. 19 (2017) 4132–4140.
[4] X. Xia, Y. Zhang, D. Chao, Q. Xiong, Z. Fan, X. Tong, J. Tu, H. Zhang, H. Jin Fan, Energy Environ. Sci. 8 (2015) 1559–1568.
[5] X. Liu, C. Ma, J. Li, B. Zielinska, R.J. Kalenczuk, X. Chen, P.K. Chu, T. Tang, E. Mijowska, J. Power Sources 412 (2019) 1–9.
[6] V. Sahu, S. Grover, B. Tulachan, M. Sharma, G. Srivastava, M. Roy, M. Saxena, N. Sethy, K. Bhargava, D. Philip, H. Kim, G. Singh, S.K. Singh, M. Das, R.K. Sharma, Electrochim. Acta 160 (2015) 244–253.
[7] C. Long, J. Zhuang, Y. Xiao, M. Zheng, H. Hu, H. Dong, B. Lei, H. Zhang, Y. Liu, J. Power Sources 310 (2016) 145–153.
[8] Y. Wang, Y. Song, Y. Wang, X. Chen, Y. Xia, Z. Shao, J. Mater. Chem. 3 (2) (2015) 773–781.
[9] Y.S. Yun, M.E. Lee, M.J. Joo, H.-J. Jin, J. Power Sources 246 (2014) 540–547.
[10] H. Yan, Y. Li, X. Guo, M. Zhou, H.Q. Wang, Y. Dai, J.C. Zheng, J. Electrochem. Soc. 165 (2018) A2075–A2083.
[11] M.P. Bichat, E. Raymundo-Pinero, F. Beguin, Carbon 48 (2010) 4351–4361.
[12] V. Subramanian, C. Luo, A.M. Stephan, K.S. Nahm, S. Thomas, B. Wei, J. Phys. Chem. C 111 (2007) 7527–7531.
[13] B. Liu, Y. Liu, H. Chen, M. Yang, H. Li, J. Power Sources 341 (2017) 309–317.
[14] R. Atchudana, T.N.J.I. Edison, S. Perumal, A.S. Parveenc, Y.R. Lee, J. Electroanal. Chem. 833 (2019) 357–369.
[15] J. Chen, H. Wei, H. Chen, W. Yao, H. Lin, S. Han, Electrochim. Acta 271 (2018) 49–57.
[16] J. Niu, J. Lianga, R. Shao, M. Liu, M. Dou, Z. Li, Y. Huang, F. Wang, Nano Energy 41 (2017) 285–292.
[17] Y.S. Yun, S.Y. Cho, J. Shim, B.H. Kim, S. Chang, S.J. Baek, Y.S. Huh, Y. Tak, Y. W. Park, S. Park, H. Jin, Adv. Mater. 25 (2013) 1993–1998.
[18] M. Ghidiu, M.R. Lukatskaya, M.Q. Zhao, Y. Gogotsi, M.W. Barsoum, Nature 516 (2014) 78–81.
[19] M. Acerce, D. Voiry, M. Chhowalla, Nat. Nanotechnol. 10 (2015) 313–318.
[20] R. Wang, P. Wang, X. Yan, J. Lang, C. Peng, Q. Xue, ACS Appl. Mater. Interfaces 4 (11) (2012) 5800–5806.
[21] M. Liu, J. Niu, Z. Zhang, M. Dou, F. Wang, Nano Energy 51 (2018) 366–372.
[22] K. Fic, G. Lota, M. Meller, E. Frackowiak, Energy Environ. Sci. 5 (2) (2012) 5842–5850.
[23] H. Cui, G. Zhu, X. Liu, F. Liu, Y. Xie, C. Yang, T. Lin, Hui Gu, F. Huang, Adv. Sci. 2 (2015) 1500126.
[24] C. Long, L. Jiang, X. Wu, Y. Jiang, D. Yang, C. Wang, T. Wei, Z. Fan, Carbon 93 (2015) 412–420.
[25] C. Long, X. Chen, L. Jiang, L. Zhi, Z. Fan, Porous layer-stacking carbon derived from in-built template in biomass for high volumetric performance supercapacitors, Nano Energy 12 (2015) 141–151.
[26] J. Liu, Y. Deng, X. Li, L. Wang, Sustain. Chem. Eng. 4 (1) (2015) 177–187.
[27] J.M. Rosas, R.R. Rosas, J.R. Mirasol, T. Cordero, Carbon 50 (4) (2012) 1523–1537.
[28] J.T. Medford, W.G. Hardin, S. Dai, K.P. Johnston, K.J. Stevenson, Nat. Mater. 13 (7) (2014) 726–732.
[29] D.P. Dubal, N.R. Chodankar, D.-H. Kim, P. Gomez-Romero, Chem. Soc. Rev. 47 (6) (2018) 2065–2129.
[30] H. Yan, J. Wang, Y. Fang, M. Zhou, X. Guo, H.-Q. Wang, Dai Yang, Wenrong Li, J.-C. Zheng, Electrochim. Acta 304 (2019) 138–145.